Functional impact of pathogenic Runt domain mutations in *Runx2* on skeletal and dental development in cleidocranial dysplasia

Saki Ogawa[1,2,*], Shinnosuke Higuchi [1,*], Yuki Yoshimoto[1,*, §], Mari Hoshino[1,3], Shigenori Miura[1], Atsuko Hamada[3], Hitomi Watanabe[4], Tetsushi Sakuma[5], Kadi Hu[1], Shun Ogata[1,2], Kenta Uchibe [6], Katsumi Fujimoto[1], Takashi Yamamoto[7], Tetsuji Okamoto[3], Ryo Kunimatsu[2], Yusuke Sotomaru[8], Kotaro Tanimoto[2], Gen Kondoh[4], Toshihisa Komori[9], Denitsa Docheva[10], and Chisa Shukunami[1]†

[1]Department of Molecular Biology and Biochemistry, Graduate School of Biomedical & Health Sciences, Hiroshima University, Hiroshima 734-8553, Japan

[2]Department of Orthodontics and Craniofacial Developmental Biology, Graduate School of Biomedical and Health Sciences, Hiroshima University, Hiroshima 734-8553, Japan

[3]Department of Oral Oncology, Graduate School of Biomedical & Health Sciences, Hiroshima University, Hiroshima 734-8553, Japan

[4]Laboratory of Integrative Biological Science, Institute for Life and Medical Sciences, Kyoto University, Kyoto 606-8507, Japan

[5]Graduate School of Agriculture, Kyoto University, Kyoto 606-8502, Japan

[6]Department of Maxillofacial Anatomy and Neuroscience, Graduate School of Biomedical & Health Sciences, Hiroshima University, Hiroshima 734-8553, Japan

[7]Division of Integrated Sciences for Life, Graduate School of Integrated Sciences for Life, Hiroshima University, Higashi-Hiroshima, Hiroshima 739-8526, Japan

[8]Natural Science Center for Basic Research and Development, Hiroshima University, Hiroshima 734-8553, Japan

[9]Department of Molecular Tumor Biology, Nagasaki University Graduate School of Biomedical Sciences, Nagasaki 852-8588, Japan

[10]Department of Musculoskeletal Tissue Regeneration, Orthopaedic Hospital König-Ludwig-Haus, Julius-Maximilians-University Würzburg, 97074 Würzburg, Germany

[§]**Present address:** Department of Molecular Craniofacial Embryology and Oral Histology, Graduate School of Medical and Dental Sciences, Institute of Science Tokyo, Tokyo 113-8510, Japan

Running title: CCD mouse model with pathogenic *Runx2* mutations

Key words: *Runx2*; Cleidocranial dysplasia; Runt domain; skeletogenesis; tooth root furcation.

*These authors contributed equally to this work

†Corresponding Author

Chisa Shukunami, DDS, Ph.D.

Department of Molecular Biology and Biochemistry, Graduate School of Biomedical and Health Sciences, Hiroshima University, Hiroshima 734-8553, Japan

Tel: +81-82-257-5628

shukunam@hiroshima-u.ac.jp

Abstract

Runt-related transcription factor 2 (RUNX2) is essential for skeletogenesis, and mutations in its gene cause cleidocranial dysplasia (CCD), an autosomal dominant skeletal disorder. The evolutionarily conserved 128-amino acid Runt homology domain (RHD) of human RUNX2 is essential for DNA binding and heterodimerization, and serves as a mutation hotspot associated with severe CCD phenotypes. To elucidate the functional impact of pathogenic RHD mutations *in vivo*, we generated two novel mouse lines: one carrying a missense mutation, c.695G>A (p.R232Q) (*Runx2*$^{m/+}$), corresponding to the human *RUNX2* c.674G>A (p.R225Q), and the other harboring a frameshift mutation, c.697_698delGA (p.E233TfsTer9) (*Runx2*$^{\Delta 2/+}$), causing a premature stop codon. Homozygous *Runx2*$^{m/m}$ and *Runx2*$^{\Delta 2/\Delta 2}$ mice lacked membranous ossification, whereas heterozygous *Runx2*$^{m/+}$ and *Runx2*$^{\Delta 2/+}$ mice displayed typical CCD-like skeletal features, including an open anterior fontanelle and clavicle hypoplasia. Unexpectedly, heterozygotes carrying pathogenic mutations in RHD developed an accessory root-like protrusion at the furcation of three-rooted maxillary first molars, representing a previously unrecognized dental phenotype during root development. Dual luciferase assays revealed impaired transactivation of the p.R232Q mutant Runx2 on the osteocalcin enhancer/promoter. Wild-type Runx2 was robustly expressed in osteoblasts and hypertrophic chondrocytes during bone formation, but the mutant Runx2 exhibited reduced expression in hypertrophic chondrocytes and partially impaired nuclear localization, resulting in arrested osteoblast and chondrocyte maturation. Our mutant mouse model provides a valuable *in vivo* platform to study CCD pathogenesis, mechanisms of tooth root furcation, and therapeutic interventions targeting dysfunctional RHD.

Introduction

Cleidocranial dysplasia (CCD; OMIM #119600) is a rare autosomal dominant skeletal and dental disorder caused by haploinsufficiency of the *Runt-related transcription factor 2* (*RUNX2*)[1,2]. CCD affects one in a million people worldwide, with no gender or ethnic differences, although mild cases may be underdiagnosed[3]. Clinical features include clavicular hypoplasia or aplasia, midfacial hypoplasia, delayed closure of cranial sutures, Wormian bones, and a persistent anterior fontanelle closure, often with short stature and dental anomalies[1]. Prolonged retention of deciduous teeth and multiple unerupted supernumerary permanent teeth are frequently encountered in dental clinics[3,4], requiring long-term multidisciplinary care, including oral and maxillofacial surgery and orthodontics, to manage function, aesthetics, and patient burden.

The human *RUNX2* and mouse *Runx2* genes comprise 8 exons, spanning approximately 218 kb (hg38, NM_001024630.4) and 206 kb. (mm39, NM001271627.2), respectively[5,6]. Homozygous *Runx2*-deficient mice die shortly after birth from respiratory failure, exhibiting a complete lack of ossification and arrested embryonic tooth development, while heterozygous mice exhibit persistent open anterior fontanelle, clavicle hypoplasia, and other skeletal abnormalities resembling human CCD[2,7]. RUNX2/Runx2 is a key transcription factor in skeletal development, regulating mesenchymal commitment to the osteoblastic lineage, proliferation and maturation of chondrocytes and osteoblasts, and transdifferentiation of hypertrophic chondrocytes into osteoblasts[8]. Intramembranous ossification strongly depends on *Runx2* and requires higher levels of its expression compared to endochondral ossification[5]. In *Runx2*$^{+/-}$ mice, as in human CCD, delayed eruption of incisors and maxillary first molars occurs due to impaired osteoclast recruitment in the alveolar bone, although neither impacted nor supernumerary teeth are present[9].

97 RUNX2 contains several functional domains, including a glutamine alanine-rich domain
98 (QA), a highly conserved Runt homology domain (RHD), which is also referred to as the Runt
99 domain, a proline serine threonine domain (PST), and a C-terminal VWRPY motif, and harbors
100 a nuclear transition signal (NLS) at the C-terminus of the RHD and a nuclear matrix targeting
101 signal (NMTS)[10]. More than 200 *RUNX2* mutations have been reported in CCD patients,
102 including frameshift, missense, nonsense, and splice-site variants[6,11]. While nonsense and
103 frameshift mutations are distributed throughout the gene, most missense mutations cluster
104 within the 128-amino acid RHD, which is critical for DNA binding and heterodimerization with
105 core-binding factor subunit β (Cbfb)[6,12,13]. Many pathogenic mutations associated with CCD,
106 especially those linked to severe dental anomalies, are missense or nonsense mutations affecting
107 the RHD[6]. However, the mechanisms by which these mutations cause severe CCD have long
108 remained unclear, owing to the absence of *in vivo* models with RHD-specific mutations and the
109 limitations of cellular systems that cannot fully recapitulate the disease complexity.
110 Recently, several disease-specific induced pluripotent stem (iPS) cell lines carrying
111 mutations such as p.R225Q, p.S124W, p.R391X, and p.Q67X have been established from
112 patients[14-16]. iPS cells harboring nonsense mutations p.Q67X in the QA domain and p.R391X
113 in the NTMS domain exhibit reduced osteogenic differentiation capacity[14]. Transplantation of
114 osteoblasts induced from p.Q67X iPS cells into rat calvarial defects led to limited bone
115 regeneration, which was rescued by genetic correction of the *RUNX2* mutation[14]. While
116 disease-specific iPS cells are useful for modeling altered differentiation potential and cellular
117 behavior *in vitro* but fail to recapitulate morphogenetic processes during development.
118 Furthermore, iPS cells from CCD patients with heterozygous *RUNX2* mutations do not allow
119 comprehensive evaluation of mutant protein function. Despite extensive studies on RUNX2
120 and CCD, the *in vivo* impact of RHD mutations is still not well characterized.

121 In this study, we generated two novel mouse models carrying RHD mutations: a missense
122 mutation (c.695G>A; p.R232Q) and a frameshift mutation (c.697_698delGA; p.E233TfsTer9).
123 These models serve as a robust platform for investigating CCD pathogenesis and uncover
124 previously unrecognized abnormalities in tooth root furcation. By enabling detailed functional
125 analysis of RHD mutations in a disease-relevant context, they provide new insights into CCD
126 pathogenesis and may contribute to the development of targeted therapies.
127

128 **Materials and methods**

129 Animals

130 C57BL/6 mice were purchased from CLEA Japan, Inc. (Tokyo, Japan) and bred for experiments.
131 Homozygous *Runx2*$^{m/m}$ and *Runx2*$^{\Delta 2/\Delta 2}$ mice exhibited perinatal lethality, which was
132 expected[7,12], and no intervention was undertaken as it was unpreventable. Mice were
133 maintained under a 12-hour light/dark cycle (lights on from 8:00 to 20:00) at 23 ± 3 ˚C and 50
134 ± 10% humidity. Animals were provided γ-irradiated MF chow (Oriental Yeast Co., Ltd., Tokyo,
135 Japan) and autoclaved water ad libitum. All procedures were approved by the Animal Care
136 Committee of the Institute for Frontier Life and Medical Sciences, Kyoto University, as well as
137 the Committee of Animal Experimentation and the Recombinant DNA Committee of
138 Hiroshima University.
139

140 Generation of TALEN-mediated *Runx2* mutant mouse lines

141 TALEN plasmids targeting mouse *Runx2* were constructed using the Platinum Gate TALEN
142 Kit (Addgene, Watertown, MA) as previously described[17]. After linearization of TALEN
143 plasmids for *Runx2-TALEN-R* and *-L* with SmaI, mRNAs were synthesized using the
144 mMESSAGE mMACHINE T7 ULTRA Kit (Thermo Fisher Scientific, Waltham, MA) and

145 purified with the MEGAclear kit (Thermo Fisher Scientific). The TALEN mRNAs and an
146 ssODN carrying the p.R232Q and a silent ApaI site were microinjected into C57BL/6 oocytes.
147 Injected eggs were transferred into pseudopregnant ICR females. Genotyping was performed
148 by PCR on genomic DNA extracted from earpieces using specific primers (Table S3). The
149 products were digested with SmaI and ApaI, and confirmed by direct sequencing using the
150 BigDye Terminator Cycle Sequencing kit and an ABI 3100 Genetic Analyzer (Applied
151 Biosystems, Thermo Fisher Scientific). Fragments were analyzed by agarose gel
152 electrophoresis or a microchip electrophoresis system for DNA/RNA analysis (MultiNA,
153 SHIMADZU, Kyoto, Japan).
154
155 Skeletal preparation
156 Whole-mount skeletal staining was performed as previously described[18]. Embryos or mice
157 were skinned, fixed in ethanol, stained with Alcian blue 8GX (Sigma-Aldrich, Merck KGaA,
158 Darmstadt, Germany), washed with ethanol, and cleared in 1% KOH. Samples were then
159 stained with 0.05% Alizarin Red S (Sigma-Aldrich) in 1% KOH, followed by additional
160 clearing in 1% KOH. Images were acquired using a MZ16 FA stereomicroscope equipped with
161 a DFC7000 T camera (Leica Microsystems (Leica), Wetzlar, Germany).
162
163 Tissue sections
164 For frozen sections, embryos were fixed in 4% paraformaldehyde (PFA) in phosphate buffered
165 saline (PFA/PBS), infiltrated with 20% sucrose/PBS, embedded in Tissue Tek O.C.T compound
166 (Sakura Finetek, Tokyo, Japan), sectioned at 4-6 μm. For paraffin sections, embryos were fixed
167 in 4% PFA/PBS, decalcified with Morse's solution[19], dehydrated, immersed in methyl

168 benzoate (Nacalai Tesque, Kyoto, Japan), embedded in paraffin (Thermo Fisher Scientific),
169 sectioned at 6 μm.
170
171 Histological staining
172 Frozen sections were stained with ALP substrate solution of TRAP/ALP Stain Kit (FUJIFILM
173 Wako Pure Chemical Corporation (FUJIFILM Wako), Osaka, Japan), or stained with 1%
174 alizarin red (Muto Pure Chemicals, Tokyo, Japan). For toluidine blue staining, deparaffinized
175 and hydrated sections were stained with 0.05% toluidine blue solution (pH 4.1; Muto Pure
176 Chemicals).
177
178 *In situ* hybridization
179 Digoxygenin (DIG)- labelled RNA probes for *Col2a1*[20], *Acan*[20], *Ihh*, *Col10a1*[21], *Runx2*[22],
180 *Spp1*[23] and *Col1a1*[24] were synthesized using a DIG RNA labelling kit (F. Hoffmann-La Roche
181 Ltd. (Roche), Basel, Switzerland). Mouse *Col2a1* and *Ihh* cDNA were amplified by RT-PCR
182 using the following primers (Table S3). Paraffin sections were deparaffinized, rehydrated and
183 treated with 10 μg/mL Proteinase K (Roche), followed by post-fixation with 4% PFA/PBS for
184 10 min. Sections were hybridized with DIG-labeled RNA probes at 65°C for 16 h, washed, and
185 incubated with anti-DIG Fab fragment conjugated with alkaline phosphatase (anti-DIG-AP;
186 Roche) and BM purple (Roche). Counterstaining was performed with eosin (Sakura Finetek).
187
188 μCT imaging
189 Mice were anesthetized with a combination of medetomidine, midazolam, and butorphanol (0.1
190 mL per 10 g body weight). Calvaria and clavicle were scanned with SkyScan1176 (Bruker,
191 Antwerp, Belgium; 17.5 μm resolution, 50 kV and 500 μA), and teeth were scanned with

192 CosmoScan GXIII (Rigaku Holdings Corporation, Tokyo, Japan; 12.9 μm resolution, 100 kV
193 and 120 μA). 3D rendering was performed using Amira software (Thermo Fisher Scientific,
194 version 2021.1).
195
196 Plasmid construction
197 Mouse Runx2 cDNA was amplified from *pSG5-mRunx2* and cloned into the EcoRI site of
198 *pcDNA-FLAG*[20] to generate *pcDNA3 Runx2 WT* using primers. Mutant vectors carrying the
199 p.R232Q, p.R232W, or p.R200X mutations (*pcDNA3 Runx2 RQ*, *RW*, and *RX*, respectively)
200 were generated by inverse-PCR with KOD Plus DNA polymerase (TOYOBO, Osaka, Japan)
201 using *pcDNA3 Runx2 WT* as the template. See Table S2 for primers.
202
203 Dual luciferase reporter assay
204 HEK293T cells (Takara Bio Inc., Shiga, Japan) were cultured in Dulbecco's modified Eagle's
205 medium with high glucose (Sigma-Aldrich) supplemented with 10% heat-inactivated-FBS
206 (Hana-Nesco Bio Corp., Osaka, Japan), 2 mM L-glutamine (FUJIFILM Wako), and 50 mg/mL
207 kanamycin (Sigma-Aldrich) at 37°C in 5% CO_2. Cells were transiently transfected with
208 *p6OSE2-luc*[25] and *pGL4.10[luc2]*, *pGL4.74[hRluc/TK]* (Promega, Madison, WI), and
209 *pcDNA3 Runx2 WT or mutant* vectors. Transfection was performed using Lipofectamine LTX
210 Reagent or Lipofectamine 3000 Reagent (Thermo Fisher Scientific). After 48 h, luciferase
211 activities were measured using the PicaGene Dual Sea Pansy Luminescence Kit (Toyo ink,
212 Tokyo, Japan) and Centro XS^3 LB 960 (Berthold Technologies, Bad Wildbad, Germany).
213
214 Western blotting

215 Forelimbs were frozen in liquid nitrogen, crashed using SK mill (SK-200, Tokken,Inc, Chiba,
216 Japan), and lysed in 8 M urea extraction buffer [8 M urea, 50 mM Tris-HCl (pH 8.0), 1 mM
217 DTT and 1 mM EDTA]. HEK293T cells were transfected with WT or mutant Runx2 vector
218 using Lipofectamine 3000 Reagent (Thermo Fisher Scientific), and lysed in 8 M urea extraction
219 buffer. Protein concentrations were determined using BCA Protein Assay Kit (Thermo Fisher
220 Scientific), and samples were mixed with 6x SDS sample buffer (Nacalai tesque, Inc., Kyoto,
221 Japan), boiled, and loaded onto a 10% SDS-polyacrylamide gels (e-PAGEL, ATTO, Tokyo,
222 Japan). Samples were separated by SDS-PAGE and transferred to PVDF membranes using
223 iBlot3 (Invitrogen). Membrane were blocked with 3% skim milk (FUJIFILM Wako) in Tris-
224 buffered saline with 0.05% Tween 20 (TBS-T), incubated with rabbit anti-Runx2 monoclonal
225 antibody (1:1250, Cell Signalling Technology, Danvers, MA) and mouse anti-β-actin
226 monoclonal antibody (1:1250, FUJIFILM Wako) overnight, then with IRDye 680RD Goat anti-
227 Rabbit IgG and IRDye 800CW Goat anti-Mouse IgG (1:15000, LI-COR, Lincoln, NE). Bands
228 were visualized using Odyssey CLx (LI-COR).
229
230 Immunostaining
231 Frozen sections were subjected to antigen retrieval in sodium citrate buffer (pH6.0) by
232 microwave heating, followed by permeabilization with 0.2% TritonX-100 (Sigma-Aldrich).
233 After blocking with 2% skim milk/PBS, sections were incubated with rabbit anti-Runx2
234 monoclonal antibody (1:1600, Cell Signaling Technology) or rabbit anti-Collagen X
235 monoclonal antibody (1:500, Abcam, Cambridge, UK) overnight, washed with PBS, and
236 incubated with Goat anti-Rabbit IgG (H+L) Highly Cross-Adsorbed Secondary antibody
237 conjugated with Alexa Fluor Plus 594 (1:500, Thermo Fisher Scientific). Nuclei were
238 counterstained with 4',6-diamidino-2-phenylindole (DAPI) (Sigma-Aldrich). Stained sections

239 were mounted using VECTASHIELD Hard-Set Mounting Medium (Vector Laboratories, Inc.,
240 Newark, CA). Images were acquired using DMRXA microscope with DFC310 FX Camera and
241 Stellaris 5 confocal laser scanning microscope (Leica).
242
243 Image analysis
244 To analyze Runx2 nuclear localization, maximum projection images were generated from
245 confocal images using LAS X software (Leica). Cells in the Col10^{+} hypertrophic cartilage layer
246 were analyzed with ImageJ software (National Institutes of Health, Bethesda, MD). Regions of
247 interest (ROIs) for whole-cell Runx2 [ROIs(r)] were defined from Runx2 signals using
248 thresholding based on the Huang algorithm[26]. Nuclear regions of interest [ROIs(d)] were
249 defined from DAPI images with thresholds set using the Default (IsoData) algorithm[27],
250 excluding ROIs smaller than 50 pixels. ROIs(r) and ROIs(d) were overlayed on Runx2 images,
251 and the respective Runx2 intensities in whole cells and nuclei were measured using Integrated
252 Density. Nuclear localization was calculated as: %Nuclear = (Runx2 intensity in nucleus/Runx2
253 intensity in the whole cell) ×100. Only cells with overlapping ROI(r) and ROI(d), confirmed
254 by visual inspection, were included. Multiple ROI(d) within one ROI(r) were summed.
255
256 Statistical analysis
257 Statistical significance between two groups was determined using Student's *t*-test or Mann-
258 Whitney U test. Comparisons among multiple groups were performed by one-way analysis of
259 variance (ANOVA) followed by Tukey's multiple comparison test. Graphpad Prism 10
260 (Dotmatics, Boston, MA, version 10. 2. 3) was used.
261

262 **Results**

263 Establishment of CCD mouse models harboring *Runx2* missense or frameshift mutations

264 The mouse *Runx2* gene, located on chromosome 17 and composed of 8 exons, is transcribed
265 from two distinct promoters: distal P1 and proximal P2, generating isoforms with different N-
266 terminal amino acid sequences[6] (Fig. 1A, Fig. S1A). The 128-amino-acid RHD crucial for
267 DNA binding, is encoded by exons 2 to 4, and the NLS by exons 4 and 5 (Fig. 1B). CCD
268 patients with a heterozygous p.R225Q mutation in human *RUNX2* show multiple
269 supernumerary teeth and membranous bone dysplasia[15,28-30]. In mouse *Runx2*, this mutation
270 corresponds to p.R232Q owing to seven additional amino acids at the N-terminus. We
271 introduced the c.695G>A (p.R232Q) mutation into the RHD of *Runx2*. To introduce the
272 mutation via homology-directed repair (HDR), we used Platinum TALENs and a single-
273 stranded oligodeoxynucleotide (ssODN) containing the c.695G>A substitution and a silent
274 ApaI site for genotyping (Fig. 1a). Microinjection of Platinum TALEN mRNAs and a designed
275 ssODN into fertilized eggs generated 51 mice, including 14 with non-homologous end joining
276 induced indels and 2 carried the HDR-mediated knock-in allele (Table S1). Lines carrying the
277 missense (*m*) or the double-nucleotide deletion (*Δ2*) mutation were established from founder
278 mice (Fig. 1C, Fig. S1A, B). In *Δ2* mutants, deletion of nucleotides 697G and 698A caused a
279 frameshift mutation, generating a premature stop codon at 241 (Fig. S1B, Fig. 1C). For
280 genotyping, SmaI digestion yielded 115 bp and 80 bp fragments for the wild-type allele, while
281 mutant alleles produced an undigested 195 bp fragment, and ApaI digestion generated 113 bp
282 and 82 bp fragments specific to the missense mutant allele (Fig. S2). Direct sequencing
283 confirmed that *Runx2*$^{m/+}$ carried both the c.690T>G silent andc.695G>A missense mutations,
284 while *Runx2*$^{\Delta 2/+}$ harbored a two-nucleotide deletion causing a premature stop codon. (Fig. 1D).
285 Thus, we successfully established two distinct CCD model mice: one with a clinically relevant

286 RHD missense mutation associated with severe CCD and another with a frameshift mutation.

287

288 Defective bone formation in homologous *Runx2* RHD-mutant mice

289 Homozygous *Runx2*$^{m/m}$ and *Runx2*$^{\Delta 2/\Delta 2}$ mice exhibited perinatal lethality, likely due to
290 respiratory failure caused by severe skeletal abnormalities, which was predictable based on
291 previous studies of *Runx2* knockout mice[7,12]. At embryonic day 18.5 (E18.5), *Runx2*$^{+/+}$,
292 *Runx2*$^{m/+}$, and *Runx2*$^{\Delta 2/+}$ embryos were similar in size and morphology, while *Runx2*$^{m/m}$ and
293 *Runx2*$^{\Delta 2/\Delta 2}$ embryos were smaller with limb shortening, facial underdevelopment, and calvarial
294 defects (Fig. S3A-E). Skeletal development at E18.5 was compared among wild-type,
295 heterozygous, and homozygous *Runx2* RHD mutants (Fig. 2A-J). In *Runx2*$^{+/+}$ embryos,
296 intramembranous ossification progressed in the calvaria and clavicles, and endochondral
297 ossification in the axial and appendicular skeletons (Fig. 2A, F, G). In *Runx2*$^{m/+}$ or *Runx2*$^{\Delta 2/+}$
298 embryos, intramembranous ossification occurred but was impaired, causing clavicle hypoplasia
299 and delayed fontanelle closure (Fig. 2B, C, H, I). In *Runx2*$^{m/m}$ or *Runx2*$^{\Delta 2/\Delta 2}$ embryos,
300 intramembranous ossification was absent, causing skull and clavicle defects, and endochondral
301 ossification was impaired, with long bones remaining mostly cartilaginous and mineralization
302 limited to the forearms and the lower legs (Fig. 2D, E, J). Forelimb calcification was more
303 delayed in *Runx2*$^{m/m}$ than in *Runx2*$^{\Delta 2/\Delta 2}$ embryos (Fig. 2D, E).

304 Histological sections of the forearm from *Runx2*$^{+/+}$, *Runx2*$^{m/+}$, *Runx2*$^{m/m}$ and *Runx2*$^{\Delta 2/\Delta 2}$
305 embryos at E18.5 were stained with toluidine blue (TB), alkaline phosphatase (ALP), and
306 Alizarin Red (AR) (Fig. 3A-C). In *Runx2*$^{+/+}$ and *Runx2*$^{m/+}$ embryos, primary ossification
307 canters formed in the diaphysis, with metachromatic cartilage present in the metaphysis and
308 epiphysis. In *Runx2*$^{m/m}$ and *Runx2*$^{\Delta 2/\Delta 2}$ embryos, the entire bone primordium consisted
309 exclusively of cartilage (Fig. 3A). ALP activity was high from the diaphysis to the metaphysis

310 in *Runx2*$^{+/+}$ and *Runx2*$^{m/+}$ embryos, but was restricted to the hypertrophic/calcified cartilage in
311 the center of the ulna and radius of *Runx2*$^{m/m}$ and *Runx2*$^{\Delta 2/\Delta 2}$ embryos (Fig. 3B). Although the
312 calcified area was smaller than the ALP^{+} area in all genotypes, in *Runx2*$^{m/m}$ and *Runx2*$^{\Delta 2/\Delta 2}$
313 embryos, both regions were markedly smaller than those in *Runx2*$^{+/+}$ and *Runx2*$^{m/+}$ embryos
314 and were confined to the central diaphysis where hypertrophic chondrocytes were present (Fig.
315 3C). Notably, calcified cartilage was smaller in *Runx2*$^{m/m}$ than in *Runx2*$^{\Delta 2/\Delta 2}$ embryos,
316 suggesting delayed cartilage maturation (Fig. 3A-C).
317 To assess chondrogenic and osteogenic marker expression, the forearm of *Runx2*$^{+/+}$,
318 *Runx2*$^{m/+}$ and *Runx2*$^{m/m}$ embryos at E18.5 were analyzed by *in situ* hybridization (Fig. 3D-J).
319 Early chondrogenic markers *Col2a1* and *Acan* were expressed in proliferating and mature
320 chondrocytes in *Runx2*$^{+/+}$, *Runx2*$^{m/+,}$ and *Runx2*$^{m/m}$ embryos (Fig. 3D, E). *Ihh* was expressed in
321 prehypertrophic chondrocytes in *Runx2*$^{+/+}$ and *Runx2*$^{m/+}$ embryos, whereas its expression was
322 only faintly detected in the central diaphysis of *Runx2*$^{m/m}$ embryos (Fig. 3F). *Col10a1* was
323 expressed in hypertrophic chondrocytes of the metaphysis in *Runx2*$^{+/+}$ and *Runx2*$^{m/+}$ embryos,
324 but only weakly detected in hypertrophic chondrocytes in the central diaphysis in *Runx2*$^{m/m}$
325 embryos (Fig. 3G). In *Runx2*$^{+/+}$ and *Runx2*$^{m/+}$ embryos, *Runx2* and *Spp1* were expressed in
326 osteoblasts, osteocytes, and chondrocytes (Fig. 3H, I). In *Runx2*$^{m/m}$ embryos, *Runx2* was faintly
327 expressed in chondrocytes and perichondrial cells, while *Spp1* was detected in a small
328 population of hypertrophic chondrocytes in the diaphysis (Fig. 3H, I). *Col1a1* was detected in
329 osteoblasts, osteocytes, cells of the periosteum and perichondrium in *Runx2*$^{+/+}$ and *Runx2*$^{m/+}$
330 embryos, but only faintly in the perichondrium of *Runx2*$^{m/m}$ embryos (Fig. 3J).
331 These findings demonstrate that RHD mutations disrupt both intramembranous and
332 endochondral ossification, emphasizing the essential role of the RHD in skeletal development.
333

334 Functional impairment of Runx2 caused by the p.R232Q mutation in the RHD

335 Wild-type and p.R232Q mutant Runx2 proteins were analyzed by Western blotting using
336 whole-cell extracts from HEK293T cells transfected with each construct (Fig. 4A).
337 Immunoblotting with an anti-RUNX2 antibody recognizing a peptide around Arg (R) at 267 of
338 human RUNX2 confirmed the expression of both wild-type and mutant Runx2, with no
339 apparent differences, although a sight size shift was observed due to the FLAG tag (Fig. 4A,
340 Fig. S4A). Next, Western blotting with the same anti-RUNX2 antibody was performed on
341 forelimb extracts from *Runx2*$^{+/+}$, *Runx2*$^{m/+}$, and *Runx2*$^{m/m}$ embryos at E18.5 to assess Runx2
342 expression (Fig. 4B, Fig. S4B). The reported molecular weights are approximately 57 kDa for
343 isoform 1 (MASNS) and 56 kDa for isoform 2 (MRIPV)[31]. Both wild-type and p.R232Q
344 mutant Runx2 showed similar sizes in HEK293T whole-cell extracts transfected with each
345 construct (Fig. 4A, Fig. S4A) and in tissue extracts from *Runx2*$^{+/+}$, *Runx2*$^{m/+}$ and *Runx2*$^{m/m}$
346 embryos, although the expression level was markedly reduced in *Runx2*$^{m/m}$ embryos compared
347 to *Runx2*$^{+/+}$ embryos (Fig 4B, Fig. S4Bb).

348 The *p6OSE2-luc* vector contains six tandem repeats of osteoblast-specific element 2 (OSE2,
349 AACCACA) from the mouse osteocalcin promoter, a Runx2 binding site, followed by a
350 minimal promoter driving firefly luciferase expression, allowing quantification of Runx2-
351 dependent transcription[25]. To evaluate the effect of RHD mutations, HEK293T cells were
352 transfected with wild-type or mutant Runx2 (p.R232Q, p.R232W, or p.R200X) (Table S2),
353 along with *p6OSE2-luc* and the *pGL4.74[hRlux/TK]* internal control, and dual luciferase assays
354 were performed (Fig. 4C). Wild-type Runx2 showed a 6.7-fold increase in transcriptional
355 activity compared to the empty vector, whereas the p.R232Q, p.R232W, or p.R200X mutants
356 exhibited activity comparable to the empty vector, indicating that missense and nonsense
357 mutations in the RHD abolish Runx2-mediated activation via OSE2 (Fig. 4C).

358 The p.R232Q mutation lies near the NLS in the C-terminal region of the RHD[32], potentially
359 affecting Runx2 nuclear translocation. To examine the impact of the mutation on intracellular
360 localizations, immunostaining was performed on sections of the ulna sections from *Runx2*$^{+/+}$
361 and *Runx2*$^{m/m}$ embryo at E18.5 using anti-Col10 and anti-Runx2 antibodies (Fig. 5A-D).
362 Consistent with the results of *in situ* hybridization (Fig. 3G, H), In *Runx2*$^{+/+}$ embryos, Col10
363 accumulated abundantly in the metaphysis and in cartilage remnants of the primary spongiosa
364 (Fig. 5A), while Runx2^{+} cells were distributed from the metaphysis to the diaphysis (Fig. 5B).
365 In *Runx2*$^{m/m}$ mice, Col10^{+} hypertrophic chondrocytes were confined to the central diaphysis
366 (Fig. 5C), and Runx2^{+} cells were more widely distributed but with markedly weaker signal
367 intensity (Fig. 5D). In hypertrophic chondrocytes of *Runx2*$^{+/+}$ embryos, Runx2 was
368 predominantly localized in the nucleus (Fig. 5E, F). In contrast, many cells in *Runx2*$^{m/m}$ embryos
369 exhibited partial nuclear translocation, but cytoplasmic localization was also observed, and
370 overall nuclear localization of Runx2 was significantly reduced (Fig. 5G, H). Quantification of
371 the nuclear-to-total Runx2 fluorescence intensity ratio revealed a significant decrease in
372 *Runx2*$^{m/m}$ embryos compared to *Runx2*$^{+/+}$ embryos (Fig. 5I, Fig. S5).
373 These results indicate that the p.R232Q mutation in the RHD impairs Runx2 function in
374 skeletal development by reducing its expression, transcriptional activation capacity, and nuclear
375 localization.
376
377 Postnatal bone abnormalities recapitulating human CCD in *Runx2*$^{m/+}$ mice
378 *Runx2*$^{m/+}$ mice showed smaller body size and length at 1 month of (Fig. 6A) and 18.3% lower
379 body weight at 4 months compared to *Runx2*$^{+/+}$ mice (Fig. 6B). Three-dimensional (3D)
380 rendering images from micro-CT (μCT) scans revealed significantly smaller clavicles in
381 *Runx2*$^{m/+}$ mice (Fig. 6C), and skeletal preparations at 3 months confirmed markedly hypoplastic

382 clavicles and scapulae compared to *Runx2*$^{+/+}$ mice (Fig. 6D).

383 To investigate postnatal changes in cranial sutures over time, skulls of *Runx2*$^{+/+}$ and
384 *Runx2*$^{m/+}$ mice were analyzed at 1, 2, and 3 months of age using μCT, and 3D rendered images
385 were examined (Fig. 6E). At 1 month, while cranial sutures of *Runx2*$^{+/+}$ mice were nearly closed,
386 those in *Runx2*$^{m/+}$ mice remained open, showing delayed closure and Wormian bones at the
387 lambdoid suture (Fig. 6E). At 2 and 3 months, the sutures in *Runx2*$^{m/+}$ mice remained open with
388 persistent closure defects and Wormian bones, indicating impaired cranial ossification (Fig. 6E).
389 Consistently, skeletal preparations at 6 months showed that *Runx2*$^{m/+}$ mice had an open anterior
390 fontanelle, impaired suture closure, a short nasal apex, and zygomatic arch dysplasia, whereas
391 *Runx2*$^{+/+}$ mice had fully closed cranial sutures (Fig. 6F).

392 Taken together, these findings demonstrate that *Runx2*$^{m/+}$ mice carrying a clinically relevant
393 RHD missense mutation develop postnatal features of severe CCD.

394

395 Formation of accessory root-like protrusions in *Runx2*$^{m/+}$ mice

396 CCD patients often exhibit delayed eruption and supernumerary teeth[1], whereas
397 supernumerary teeth are absent in heterozygous *Runx2*-deficient mice[12]. Similarly, no
398 supernumerary teeth were observed in *Runx2*$^{m/+}$ mice; however, 3D rendering of μCT images
399 revealed a previously unreported accessory root-like protrusion between the three roots of the
400 maxillary first molars (Fig. 7A-D).

401 In mice, the maxillary first molars develop two buccal roots (mesial and distal) and one
402 palatal root, with root development coordinated through the independent growth of each root
403 from the furcation area via Hartwig's epithelial root sheath (HERS)[33]. The furcation process
404 of the mouse maxillary first molar begins with the formation of the distal buccal and palatal
405 root, followed by separation of the mesial buccal root and palatal roots, mediated through the

406 fusion of epithelial tongue-like processes formed by HERS[33]. To examine the development of
407 the small root-like protrusion, 3D μCT images of the maxillary first molars of *Runx2*$^{m/+}$ mice
408 were analyzed at 2, 3, 4, and 8 weeks (Fig. 7E-I). At 2 weeks, crown formation was complete,
409 but calcification at the root furcation area was incomplete, and three roots were not yet fully
410 separated (Fig. 7E, F). By 4 weeks, roots were clearly separated and elongated rapidly, with a
411 small protrusion forming near the furcation between the distal buccal and palatal roots (Fig.
412 7G-J). At 8 weeks, root elongation continued, but the protrusion size remained unchanged (Fig.
413 7 K, L). Figure 7M illustrates the phenotype observed in this study alongside previous findings
414 in wild-type mice[33-35], and shows that in *Runx2*$^{m/+}$ mice, the epithelial processes fail to close
415 properly during root furcation, causing a small protrusion.
416 Hence, these results identify a previously unrecognized dental phenotype associated with
417 *Runx2* haploinsufficiency and provide new insights into the molecular mechanism underlying
418 root furcation.
419
420 **Discussion**
421 This study presents the first *in vivo* functional analysis of pathological *Runx2* RHD mutations
422 using novel mouse lines carrying either a missense or a frameshift-induced dysfunctional RHD.
423 Clinically relevant *Runx2*$^{m/+}$ mice harboring p.R232Q corresponding human RUNX2 p.R225Q,
424 exhibited skeletal abnormalities characteristic of classic CCD. Notably, this is the first *in vivo*
425 evidence that homozygous RHD mutations alone can completely abolish bone formation,
426 resulting in a skeleton composed entirely of cartilage. Although supernumerary teeth were
427 absent in heterozygous mutants, 3D μCT imaging revealed a novel accessory root-like
428 protrusion in the maxillary first molar during furcation. These findings demonstrate the
429 importance of modeling specific RHD mutations and provide new insights into the skeletal and

430 dental pathology of CCD beyond previous studies of *Runx2*-deficient mice.

431 Missense substitutions account for nearly half of all mutations reported in the Human
432 Gene Mutation Database[36]. Missense mutation p.R225Q is one of the most frequent across
433 diverse populations worldwide[12,15,28,37,38]. Arginine (R) residues, such as R225 in human
434 RUNX2 is crucial for protein stability through hydrogen bonds and salt bridges. Substitutions
435 of these residues can disrupt interactions with charged molecules like DNA and other proteins,
436 leading to pathogenic effects[39]. *In silico* analysis predicts that R225, a highly conserved
437 residue across species, forms two hydrogen bonds with E226, which are lost in mutant
438 RUNX2[38]. Consistently, the equivalent mouse mutation p.R232Q abolishes osteocalcin
439 promoter activation due to loss of RHD function. In homozygous mice, expression of
440 *Col10a1*[22], a direct Runx2 target, was markedly reduced. The p.R232Q Runx2 failed to sustain
441 *Runx2* expression in hypertrophic chondrocytes, causing maturational arrest. In *Runx2*$^{\Delta 2/\Delta 2}$ mice,
442 the lack of bone formation results from loss of function, most likely due to nonsense-mediated
443 decay triggered by the frameshift mutation, consistent with previous reports that nonsense or
444 frameshift mutations also cause classic CCD[5,40,41].

445 Two *Runx2* knockout mouse lines have been previously reported: one generated by
446 disrupting the Q/A repeat domain with an *IRES-lacZ-pA* cassette[12], and another by deleting an
447 exon containing 41 amino acids of the RHD using a *PGK-neo* cassette[7]. In the latter line
448 carrying a LacZ reporter, X-gal staining showed persistent activity of the endogenous *Runx2*
449 promoter even in homozygotes, with blue staining in bone-forming regions[12]. However, the
450 prolonged half-life of LacZ hampers accurate tracking of the temporal dynamics of mutant
451 Runx2 expression during skeletogenesis. Indeed, *Runx2*$^{m/m}$ embryos exhibited markedly
452 reduced mutant Runx2 expression, suggesting that loss of functional Runx2 impairs either the
453 maintenance of its transcription or protein stability. These findings shed light on the *in vivo*

454 regulation and dynamics of Runx2 expression that are not captured by reporter-based
455 approaches.

456 The classical NLS typically comprises 5-20 amino acids rich in basic amino acid residues
457 like lysine (K) and arginine (R)[42]. Runx2 contains a Myc-related 9 amino acid NLS
458 (PRRHRQKLD) at the RHD-PST junction, essential for its nuclear localization[32]. Previous
459 studies using NIH-3T3, U2OS, C3H10T1/2, and HEK293T cells showed that wild-type
460 RUNX2 localizes to the nucleus, whereas p.R225Q or p.R225W mutants exhibited impaired
461 nuclear translocation[37,43]. Fusion proteins carrying p.R225Q or p.R225W mutation fail to
462 efficiently accumulate in the nucleus[37], unlike the wild-type. RUNX2 carrying either the
463 p.K218N or p.K220I mutation (previously described as K204N and T206I, respectively), both
464 located near the NLS, fails to translocate to the nucleus. In contrast, the p.R225Q mutant
465 (previously described as R211Q) shows approximately equal distribution between the nucleus
466 and cytoplasm in about half of the cells[43]. Although R232 in mouse Runx2 is located near the
467 NLS, its mutation caused only a partial defect in nuclear localization, with approximately 70%
468 of the mutant Runx2 detected in the nuclei of hypertrophic chondrocytes in *Runx2*$^{m/m}$ mice.
469 Thus, reduced function and expression due to RHD dysfunction, rather than impaired nuclear
470 localization, is likely the primary contributor to the skeletal phenotype. A missense mutation in
471 the RHD has been reported to exert a dominant-negative effect[44], which may explain the
472 observation that the mineralized area is smaller in missense mutant compared to the frameshift
473 mutant.

474 In CCD patients, supernumerary teeth most commonly develop in the incisors and
475 premolars[45]. In contrast, mice have a monomorphic dentition with one continuously growing
476 incisor and three molars, separated by a toothless diastema, lacking canines or premolars[46].
477 Unlike the dimorphic dentition of humans, tooth eruption in *Runx2*-deficient mice is only

478 slightly delayed or not significantly affected[9,47], similar to the normal eruption of deciduous
479 teeth in CCD patients[2,48]. These species-specific differences in dental architecture may explain
480 why the dental phenotype in mice is less pronounced than the skeletal phenotype.

481 We identified an accessory root-like protrusion in the maxillary first molars of *Runx2*$^{m/+}$
482 mice, representing a novel dental phenotype distinct from previously reported abnormalities
483 such as short roots or taurodontism[49]. In normal maxillary molars, horizontal differential
484 growth of HERS forms three tongue-like interradicular processes that fuse to divide the single
485 cervical opening into three parts, initiating multi-root formation[33,50]. The accessory roots likely
486 result from impaired fusion of these processes at the leading edge of HERS, caused by *Runx2*
487 haploinsufficiency (Fig. 7M). As Runx2 is critical for epithelial-mesenchymal interactions
488 during root development, reduced expression may disrupt spatiotemporal regulation of HERS
489 fusion during furcation, leading to protrusion formation. Notably, this protrusion was much
490 smaller than normal roots, suggesting incomplete root elongation, possibly due to aberrant
491 odontoblast differentiation. Given that maxillary first molars normally have three roots and the
492 most complex furcation among molars, their intricate morphology and spongy maxillary bone
493 structure may underlie susceptibility to furcation abnormalities in *Runx2*$^{m/+}$ mice.

494 In conclusion, our *Runx2* mutant mice replicate key skeletal features of CCD and uncover
495 a novel dental phenotype characterized by accessory roots, likely resulting from impaired root
496 furcation. Although unconfirmed in humans, homozygous mutants in mice exhibited a complete
497 lack of bone formation. These findings highlight the critical role of the RHD in both skeletal
498 and multi-root development, providing new insights into CCD pathogenesis.

499

500 **Data availability**

501 All data associated with this study are available upon request.

Acknowledgements

Plasmids for mouse *Col10a1* and *Spp1* were generously provided by Dr. Bjorn R Olsen (Harvard Medical School) and Dr. Shinsuke Ohba (Osaka University), respectively. The *p6OSE2-luc* vector was obtained from Dr. Karsenty (Columbia University) through Dr. Kenji Hata (Osaka University). We thank Drs. Kosuke Hosoba and Xynyi Yu for their technical assistance. Parts of this work was performed using the facilities at the Natural Science Center for Basic Research and Development and the Central Laboratory, Faculty of Dentistry, Hiroshima University. This study was supported by the Japan Society for the Promotion of Science Grants-in-Aid for Scientific Research (Grant Numbers: 16K15780, 21KK0161, 22K10148, 25K13145); the Frontier Development Program for Genome Editing funded by the Doctoral Program for Worldleading Innovative and Smart Education, JST SPRING (Grant Number JPMJSP2132); and the Cooperative Research Program of the Institute for Frontier Life and Medical Sciences, Kyoto University, Japan.

Competing interests

The authors declare no competing or financial interests.

Author contributions

C.S. designed the research; S.Ogawa, S.H., Y.Y., M.H., C.S., A.H., H.W., T.S., K.H., S.Ogata, K.F., and G.K. performed the experiments; C.S., S.Ogawa, S.H., Y.Y., A.H., S.M., and T.S. analyzed data; C.S., S.Ogawa, S.H., and Y.Y. wrote the paper; C.S., S.M., K.U., T.O., K.T., T.K., and D.D. provided feedback and guidance; S.M., A.H., T.S., K.F., T.O., T.Y., R.K., Y.S., and D.D. reviewed and edited the manuscript.

526

527 **References**

528 1. Mundlos S. Cleidocranial dysplasia: clinical and molecular genetics. J Med Genet.
529 1999;36(3):177-82.
530 2. Mundlos S, Otto F, Mundlos C, et al. Mutations involving the transcription factor
531 CBFA1 cause cleidocranial dysplasia. Cell. 1997;89(5):773-9.
532 https://doi.org/10.1016/s0092-8674(00)80260-3
533 3. Cooper SC, Flaitz CM, Johnston DA, et al. A natural history of cleidocranial dysplasia.
534 Am J Med Genet. 2001;104(1):1-6. https://doi.org/10.1002/ajmg.10024
535 4. Kreiborg S, Jensen BL. Tooth formation and eruption - lessons learnt from cleidocranial
536 dysplasia. Eur J Oral Sci. 2018;126 Suppl 1:72-80. https://doi.org/10.1111/eos.12418
537 5. Lou Y, Javed A, Hussain S, et al. A Runx2 threshold for the cleidocranial dysplasia
538 phenotype. Human Molecular Genetics. 2009;18(3).
539 https://doi.org/10.1093/hmg/ddn383
540 6. Jaruga A, Hordyjewska E, Kandzierski G, et al. Cleidocranial dysplasia and RUNX2-
541 clinical phenotype-genotype correlation. Clin Genet. 2016;90(5):393-402.
542 https://doi.org/10.1111/cge.12812
543 7. Komori T, Yagi H, Nomura S, et al. Targeted disruption of Cbfa1 results in a complete
544 lack of bone formation owing to maturational arrest of osteoblasts. Cell. 1997;89(5).
545 https://doi.org/10.1016/S0092-8674(00)80258-5
546 8. Komori T. Whole Aspect of Runx2 Functions in Skeletal Development. Int J Mol Sci.
547 2022;23(10). https://doi.org/10.3390/ijms23105776

548 9. Yoda S, Suda N, Kitahara Y, et al. Delayed tooth eruption and suppressed osteoclast
549 number in the eruption pathway of heterozygous Runx2/Cbfa1 knockout mice. Archives
550 of Oral Biology. 2004;49(6). https://doi.org/10.1016/j.archoralbio.2004.01.010
551 10. Bruderer M, Richards RG, Alini M, et al. Role and regulation of RUNX2 in osteogenesis.
552 Eur Cell Mater. 2014;28:269-86. https://doi.org/10.22203/ecm.v028a19
553 11. Yang L, Lu G, Shen W, et al. Whole-exome sequencing of a novel initiation codon
554 mutation in RUNX2 in a Chinese family with cleidocranial dysplasia. Medicine
555 (Baltimore). 2021;100(45):e27746. https://doi.org/10.1097/MD.0000000000027746
556 12. Otto F, Thornell AP, Crompton T, et al. Cbfa1, a candidate gene for cleidocranial
557 dysplasia syndrome, is essential for osteoblast differentiation and bone development.
558 Cell. 1997;89(5). https://doi.org/10.1016/S0092-8674(00)80259-7
559 13. Yoshida T, Kanegane H, Osato M, et al. Functional analysis of RUNX2 mutations in
560 cleidocranial dysplasia: novel insights into genotype-phenotype correlations. Blood
561 Cells Mol Dis. 2003;30(2):184-93. https://doi.org/10.1016/s1079-9796(03)00020-2
562 14. Saito A, Ooki A, Nakamura T, et al. Targeted reversion of induced pluripotent stem cells
563 from patients with human cleidocranial dysplasia improves bone regeneration in a rat
564 calvarial bone defect model. Stem Cell Res Ther. 2018;9(1):12.
565 https://doi.org/10.1186/s13287-017-0754-4
566 15. Yamasaki S, Hamada A, Akagi E, et al. Generation of cleidocranial dysplasia-specific
567 human induced pluripotent stem cells in completely serum-, feeder-, and integration-
568 free culture. In Vitro Cellular and Developmental Biology - Animal. 2016;52(2).
569 https://doi.org/10.1007/s11626-015-9968-x

570 16. Hamada A, Mukasa H, Taguchi Y, et al. Identification of a familial cleidocranial
571 dysplasia with a novel RUNX2 mutation and establishment of patient-derived induced
572 pluripotent stem cells. Odontology. 2022;110(3):444-51.
573 https://doi.org/10.1007/s10266-021-00674-5
574 17. Sakuma T, Ochiai H, Kaneko T, et al. Repeating pattern of non-RVD variations in DNA-
575 binding modules enhances TALEN activity. Sci Rep. 2013;3:3379.
576 https://doi.org/10.1038/srep03379
577 18. Rigueur D, Lyons KM. Whole-mount skeletal staining. Methods Mol Biol.
578 2014;1130:113-21. https://doi.org/10.1007/978-1-62703-989-5_9
579 19. Shibata Y, Fujita S, Takahashi H, et al. Assessment of decalcifying protocols for
580 detection of specific RNA by non-radioactive in situ hybridization in calcified tissues.
581 Histochem Cell Biol. 2000;113(3):153-9. https://doi.org/10.1007/s004180050434
582 20. Takimoto A, Kokubu C, Watanabe H, et al. Differential transactivation of the upstream
583 aggrecan enhancer regulated by PAX1/9 depends on SOX9-driven transactivation. Sci
584 Rep. 2019;9(1):4605. https://doi.org/10.1038/s41598-019-40810-4
585 21. Apte SS, Seldin MF, Hayashi M, et al. Cloning of the human and mouse type X collagen
586 genes and mapping of the mouse type X collagen gene to chromosome 10. Eur J
587 Biochem. 1992;206(1):217-24. https://doi.org/10.1111/j.1432-1033.1992.tb16919.x
588 22. Inada M, Yasui T, Nomura S, et al. Maturational disturbance of chondrocytes in Cbfa1-
589 deficient mice. Dev Dyn. 1999;214(4):279-90. https://doi.org/10.1002/(SICI)1097-
590 0177(199904)214:4<279::AID-AJA1>3.0.CO;2-W
591 23. Bastepe M, Weinstein LS, Ogata N, et al. Stimulatory G protein directly regulates

592 hypertrophic differentiation of growth plate cartilage in vivo. Proc Natl Acad Sci U S
593 A. 2004;101(41):14794-9. https://doi.org/10.1073/pnas.0405091101
594 24. Yoshimoto Y, Takimoto A, Watanabe H, et al. Scleraxis is required for maturation of
595 tissue domains for proper integration of the musculoskeletal system. Scientific Reports.
596 2017.
597 25. Ducy P, Zhang R, Geoffroy V, et al. Osf2/Cbfa1: a transcriptional activator of osteoblast
598 differentiation. Cell. 1997;89(5):747-54. https://doi.org/10.1016/s0092-
599 8674(00)80257-3
600 26. Huang L-K, Wnag M-JJ. Image thresholding by minimizing the measures of fuzziness.
601 Pattern Recognition. 1995;28(1):41-51. https://doi.org/10.1016/0031-3203(94)E0043-
602 K
603 27. Ridler TW, Calvard S. Picture Thresholding using an iterative selection method. IEEE
604 Transactions on Systems, Man, and Cybernetics. 1978;8(8):630-2.
605 https://doi.org/10.1109/TSMC.1978.4310039
606 28. Wu LZ, Su WQ, Liu YF, et al. Role of the RUNX2 p.R225Q mutation in cleidocranial
607 dysplasia: A rare presentation and an analysis of the RUNX2 protein structure. Genetics
608 and Molecular Research. 2014;13(1). https://doi.org/10.4238/2014.February.27.3
609 29. Lee KE, Seymen F, Ko J, et al. RUNX2 mutations in cleidocranial dysplasia. Genet Mol
610 Res. 2013;12(4):4567-74. https://doi.org/10.4238/2013.October.15.5
611 30. Suda N, Hattori M, Kosaki K, et al. Correlation between genotype and supernumerary
612 tooth formation in cleidocranial dysplasia. Orthod Craniofac Res. 2010;13(4):197-202.
613 https://doi.org/10.1111/j.1601-6343.2010.01495.x

614 31. Brubaker KD, Vessella RL, Brown LG, et al. Prostate cancer expression of runt-domain
615 transcription factor Runx2, a key regulator of osteoblast differentiation and function.
616 Prostate. 2003;56(1):13-22. https://doi.org/10.1002/pros.10233
617 32. Thirunavukkarasu K, Mahajan M, McLarren KW, et al. Two domains unique to
618 osteoblast-specific transcription factor Osf2/Cbfa1 contribute to its transactivation
619 function and its inability to heterodimerize with Cbfbeta. Mol Cell Biol.
620 1998;18(7):4197-208. https://doi.org/10.1128/MCB.18.7.4197
621 33. Li J, Parada C, Chai Y. Cellular and molecular mechanisms of tooth root development.
622 Development. 2017;144(3):374-84. https://doi.org/10.1242/dev.137216
623 34. Fujita Y. Formation of subpulpal wall in mouse maxillary first molar. Jpn J Oral Biol.
624 1978;20:221-8. (in Japanease)
625 35. Seo H, Kim J, Hwang JJ, et al. Regulation of root patterns in mammalian teeth. Sci Rep.
626 2017;7(1):12714. https://doi.org/10.1038/s41598-017-12745-1
627 36. Stenson PD, Mort M, Ball EV, et al. The Human Gene Mutation Database: towards a
628 comprehensive repository of inherited mutation data for medical research, genetic
629 diagnosis and next-generation sequencing studies. Hum Genet. 2017;136(6):665-77.
630 https://doi.org/10.1007/s00439-017-1779-6
631 37. Quack I, Vonderstrass B, Stock M, et al. Mutation analysis of core binding factor A1 in
632 patients with cleidocranial dysplasia. Am J Hum Genet. 1999;65(5):1268-78.
633 https://doi.org/10.1086/302622
634 38. López JT, Martinez SG, Rivera Vega MdR, et al. New Genetic Variants of RUNX2 in
635 Mexican Families Cause Cleidocranial Dysplasia. Biology. 2024;13.

636 39. Pandey P, Alexov E. Most Monogenic Disorders Are Caused by Mutations Altering
637 Protein Folding Free Energy. Int J Mol Sci. 2024;25(4).
638 https://doi.org/10.3390/ijms25041963
639 40. Xuan D, Sun X, Yan Y, et al. Effect of cleidocranial dysplasia-related novel mutation of
640 RUNX2 on characteristics of dental pulp cells and tooth development. J Cell Biochem.
641 2010;111(6):1473-81. https://doi.org/10.1002/jcb.22875
642 41. Huang Y, Song Y, Zhang C, et al. Novel RUNX2 frameshift mutations in Chinese
643 patients with cleidocranial dysplasia. Eur J Oral Sci. 2013;121(3 Pt 1):142-7.
644 https://doi.org/10.1111/eos.12048
645 42. Dingwall C, Laskey RA. Nuclear targeting sequences--a consensus? Trends Biochem
646 Sci. 1991;16(12):478-81. https://doi.org/10.1016/0968-0004(91)90184-w
647 43. Yoshida T, Kanegane H, Osato M, et al. Functional analysis of RUNX2 mutations in
648 Japanese patients with cleidocranial dysplasia demonstrates novel genotype-phenotype
649 correlations. Am J Hum Genet. 2002;71(4):724-38. https://doi.org/10.1086/342717
650 44. Puppin C, Pellizzari L, Fabbro D, et al. Functional analysis of a novel RUNX2 missense
651 mutation found in a family with cleidocranial dysplasia. J Hum Genet.
652 2005;50(12):679-83. https://doi.org/10.1007/s10038-005-0311-3
653 45. Lu Y, Wang J, Li L, et al. Three-dimensional evaluation of dental characteristics in
654 patients with Cleidocranial dysplasia. BMC Oral Health. 2024;24(1):572.
655 https://doi.org/10.1186/s12903-024-04353-z
656 46. Peterkova R, Lesot H, Peterka M. Phylogenetic memory of developing mammalian
657 dentition. J Exp Zool B Mol Dev Evol. 2006;306(3):234-50.

https://doi.org/10.1002/jez.b.21093

47. Zou SJ, D'Souza RN, Ahlberg T, et al. Tooth eruption and cementum formation in the Runx2/Cbfa1 heterozygous mouse. Arch Oral Biol. 2003;48(9):673-7. https://doi.org/10.1016/s0003-9969(03)00135-3

48. Jensen BL, Kreiborg S. Development of the dentition in cleidocranial dysplasia. J Oral Pathol Med. 1990;19(2):89-93. https://doi.org/10.1111/j.1600-0714.1990.tb00803.x

49. Wang J, Feng JQ. Signaling Pathways Critical for Tooth Root Formation. J Dent Res. 2017;96(11):1221-8. https://doi.org/10.1177/0022034517717478

50. Kumar GS. Development and grwoth of Teeth. In: Kumar GS, editor. Orban's Oral Histology and Embryology. Haryana, India: Elsevier; 2019.

671 **Figure legends**

672 **Fig. 1.** Generation of *Runx2* mutant mice using Platinum TALENs.

673 (A) Schematic representation of the mouse *Runx2* gene with eight exons (labeled E1-E8 below),
674 distal (P1) and proximal (P2) promoters for Type II (MASNSL) and Type I (MRIVD) isoforms,
675 and target sites of Platinum TALENs (*mRunx2-TALEN-L* and *-R*). A 10 kb scale bar is shown.
676 The SmaI site (red box) includes G695 (underlined). The ssODN contains target sites (green),
677 a T>G silent mutation at 690 creating an ApaI site (blue box), and a G>A mutation at 695
678 disrupting the SmaI site. (B) Domain structure of the mRunx2 Type II protein (528 aa) and its
679 corresponding exons. The protein comprises a QA repeat domain, RHD, NLS, PST-rich domain,
680 NMTS, and a C-terminal VWRPY motif. Amino acid positions are indicated above, and the
681 corresponding exons (E1-E8) are shown below. (C) Nucleotide sequences are shown for the
682 wild-type (*Wt*, 670-725), missense mutant (*m*, c.695G>A; p.R232Q, 670-725), and two-base
683 deletion (*Δ2*, c.697_698delGA; p.E233TfsTer9, 670-723) alleles. *Wt* is on top, *m* in the middle,
684 and *Δ2* at the bottom. (D) Representative electropherograms of the targeted *Runx2* region in
685 $Runx2^{+/+}$, $Runx2^{m/+}$, and $Runx2^{\Delta 2/+}$ mice. A black arrow marks T at 690 in $Runx2^{+/+}$and
686 $Runx2^{m/+}$ mice. A blue arrow indicates overlapping T and A peaks at 690 in $Runx2^{m/+}$ mice, and
687 a red arrow shows overlapping A and G peaks at position 695 in $Runx2^{m/+}$ mice.

688

689 **Fig. 2.** Skeletal phenotypes of *Runx2* mutant mice.

690 (A-J) Skeletal preparations of $Runx2^{+/+}$ (A, F, G), $Runx2^{m/+}$ (B, H, I), $Runx2^{\Delta 2/+}$ (C), $Runx2^{m/m}$
691 (D, J), and $Runx2^{\Delta 2/\Delta 2}$ (E) mice at E18.5. Lateral views of embryos (A-E), clavicles (G, I) and
692 dorsal views of the calvaria (F, H, J) are presented. A white arrow indicates weak calcification.
693 Scale bars, 2 mm.

694

695 **Fig. 3.** Histology and *in situ* hybridization of forearms in wild-type and *Runx2* mutant mice.
696 (A-C) TB, ALP, and AR staining of forearms prepared from *Runx2*$^{+/+}$, *Runx2*$^{m/+}$, *Runx2*$^{m/m}$ and
697 *Runx2*$^{\Delta 2/\Delta 2}$ embryos at E18.5. (D-J) Expression of *Col2a1* (D), *Acan* (E), *Ihh* (F), *Col10a1* (G),
698 *Runx2* (H), *Spp1* (I), and *Col1a1* (J) in the forearm of *Runx2*$^{+/+}$, *Runx2*$^{m/+}$, or *Runx2*$^{m/m}$ embryos
699 at E18.5. Blue arrowheads in (F), (G), and (I) mark prehypertrophic/hypertrophic chondrocytes.
700 A red arrowhead in (H) indicates the perichondrium. Scale bars, 500 μm.
701
702 **Fig. 4.** Expression and transcriptional activity of wild-type and mutant Runx2.
703 (A) Expression of wild-type and missense mutant Runx2 in HEK293T cells. Cells were
704 transfected with an empty vector as the control, wild-type *Runx2,* or the *Runx2 RQ* mutant
705 construct, all using the pcDNA3 vector. (B) Expression of Runx2 in forelimb extracts from
706 *Runx2*$^{+/+}$, *Runx2*$^{m/+}$ and *Runx2*$^{m/m}$ mice at E18.5. β-Actin was used as a loading control in both
707 (A) and (B). (C) Dual luciferase assay in HEK293T cells co-transfected with the *p6OSE2-luc*
708 reporter vector and either empty vector, *Runx2 WT, Runx2 RQ, RW, or RX* mutant constructs
709 using the *pcDNA3 vector*. *pGL4.74[hRluc/TK]* was also co-transfected for normalization.
710 Values for each of five wells were normalized to *pGL4.74[hRluc/TK]* and are shown as fold
711 induction relative to the empty vector. Data present one of ≧3 independent experiments (mean
712 ± SD, n = 3). ****$P < 0.0001$ *vs. Runx2 WT.*
713
714 **Fig. 5.** Altered expression and subcellular localization of mutant Runx2 in chondrocytes.
715 (A-D) Immunostaining of Col10 (A, C) and Runx2 (B, D) proteins in the ulna of *Runx2*$^{+/+}$ and
716 *Runx2*$^{m/m}$ embryos at E18.5. Nuclei are counterstained with DAPI. Yellow boxes in (A) and (**C**)
717 indicate the Col10^{+} prehypertrophic/hypertrophic cartilage zone. The corresponding regions to
718 them are shown in the semi-serial sections in (B) and (D). The number of cells in the yellow

719 boxes of (A) and (C) indicating Col10^{+} region differs between *Runx2*$^{+/+}$ and *Runx2*$^{m/m}$. (E-H)
720 Confocal images of wild-type and mutant Runx2 (red) and nuclei (blue) in
721 prehypertrophic/hypertrophic chondrocytes. Representative localization patterns of wild-type
722 (E, F) and mutant (G, H) Runx2 are highlighted by rectangles and shown in insets. (I) Nuclear
723 localization rate of Runx2 in chondrocytes of the ulna in *Runx2*$^{+/+}$ and *Runx2*$^{m/m}$ embryos.
724 Runx2 signal intensities in the whole-cell (dashed regions in f and h) and those in nucleus were
725 quantified using imageJ. Data are means ± SD (*Runx2*$^{+/+}$, n = 88 cells; *Runx2*$^{m/m}$, n = 45 cells).
726 ****$P < 0.0001$ (Mann-Whitney *U*-test). Scale bars, 200 µm (A-D), 50 µm (E-H).
727
728 **Fig. 6.** Postnatal skeletal development in *Runx2*$^{+/+}$ and *Runx2*$^{m/+}$ mice.
729 (A) Gross appearance of *Runx2*$^{+/+}$ and *Runx2*$^{m/+}$ mice at P30. (B) Body weight of *Runx2*$^{+/+}$ and
730 *Runx2*$^{m/+}$ mice at 16 weeks (n = 3). *$P < 0.05$ *vs.* *Runx2*$^{+/+}$ (unpaired Student's *t*-test). (C) µCT-
731 based 3D reconstruction images of the axial and appendicular skeleton in the upper body of 3-
732 month-old *Runx2*$^{+/+}$ and *Runx2*$^{m/+}$ mice. (D) Skeletal preparations of the pectoral girdle and
733 upper limb in *Runx2*$^{+/+}$ and *Runx2*$^{m/+}$ mice at 6 months. € µCT-based 3D reconstruction images
734 of the calvaria in *Runx2*$^{+/+}$ and *Runx2*$^{m/+}$ mice at 1, 2, and 3 months. (F) Skeletal preparations
735 of the skull from *Runx2*$^{+/+}$ and *Runx2*$^{m/+}$ mice at 6 months. Abbreviations: sc, scapula; cl,
736 clavicle; hu, humerus; f, frontal bone; p, parietal bone; ip, interparietal bone; o, occipital bone.
737 Scale bars, 5 mm.
738
739 **Fig. 7.** Dental phenotypes of postnatal *Runx2* missense mice.
740 (A-D) 3D µCT images of the maxilla and mandible in *Runx2*$^{+/+}$ and *Runx2*$^{m/+}$ mice at 3 months.
741 Panels (A) and (C) show whole jaw views. Panels (B) and (D) show slice images with overlayed
742 3D reconstructions of the maxillary first molar. Insets display enlarged views of the molars. A

743 red arrow in (D) indicates an additional root-like structure. Scale bars, 2 mm. (E-L) 3D μCT
744 images of the right maxillary first molars in *Runx2*$^{m/+}$ mice at 2, 3, 4, and 8 weeks. Axial (E, G,
745 I, K) and corresponding sagittal (F, H, J, L) views from the same individuals are shown. Orange
746 lines in axial panels indicate the sagittal section planes. Directional arrows indicate the palatal
747 (p), buccal (b), apical (a), occlusal (o), distal (d) and mesial (m) directions. Images are from the
748 same individuals (n = 3). (M) Schematic illustration of root furcation in *Runx2*$^{+/+}$ and *Runx2*$^{m/+}$
749 mice. Horizontal (top) and sagittal (bottom) views are shown, with orange lines in (E-K)
750 indicating the sagittal section planes. Tissue types are presented by pattern-filled squares. The
751 green panel shows the fusion of three epithelial processes (two buccal and one palatal) at P9,
752 P11, and P12. The blue and pink panels depict the progression of root furcation at 2, 3, and 4
753 weeks in *Runx2*$^{+/+}$ and *Runx2*$^{m/+}$ mice, respectively.

Figure 1

A

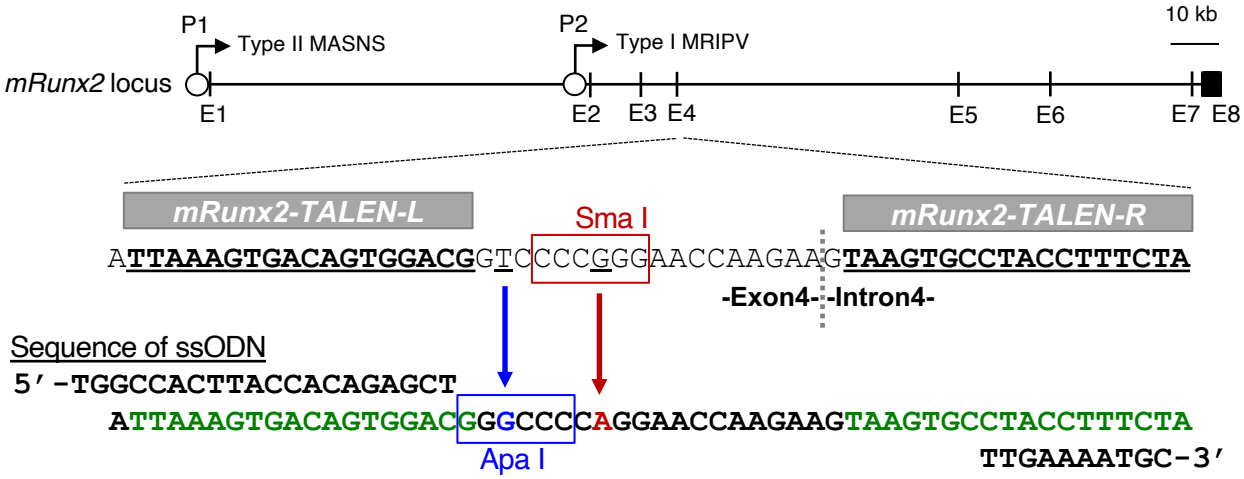

B

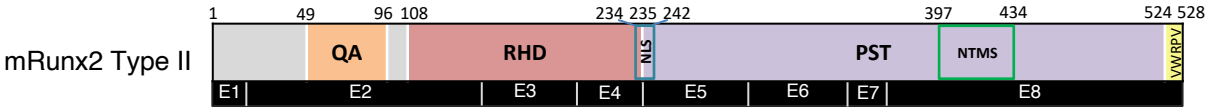

C

D

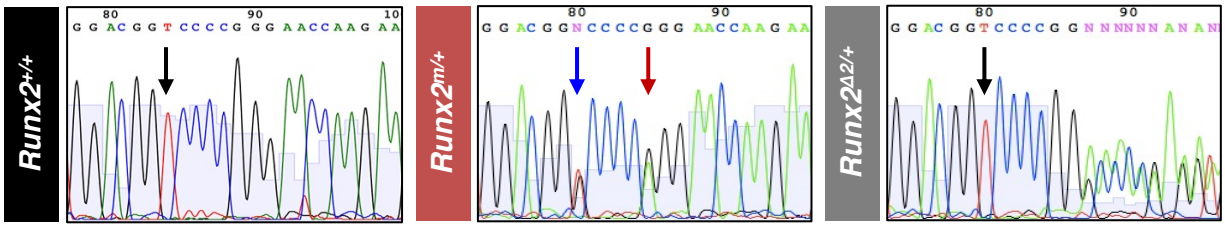

Figure 2

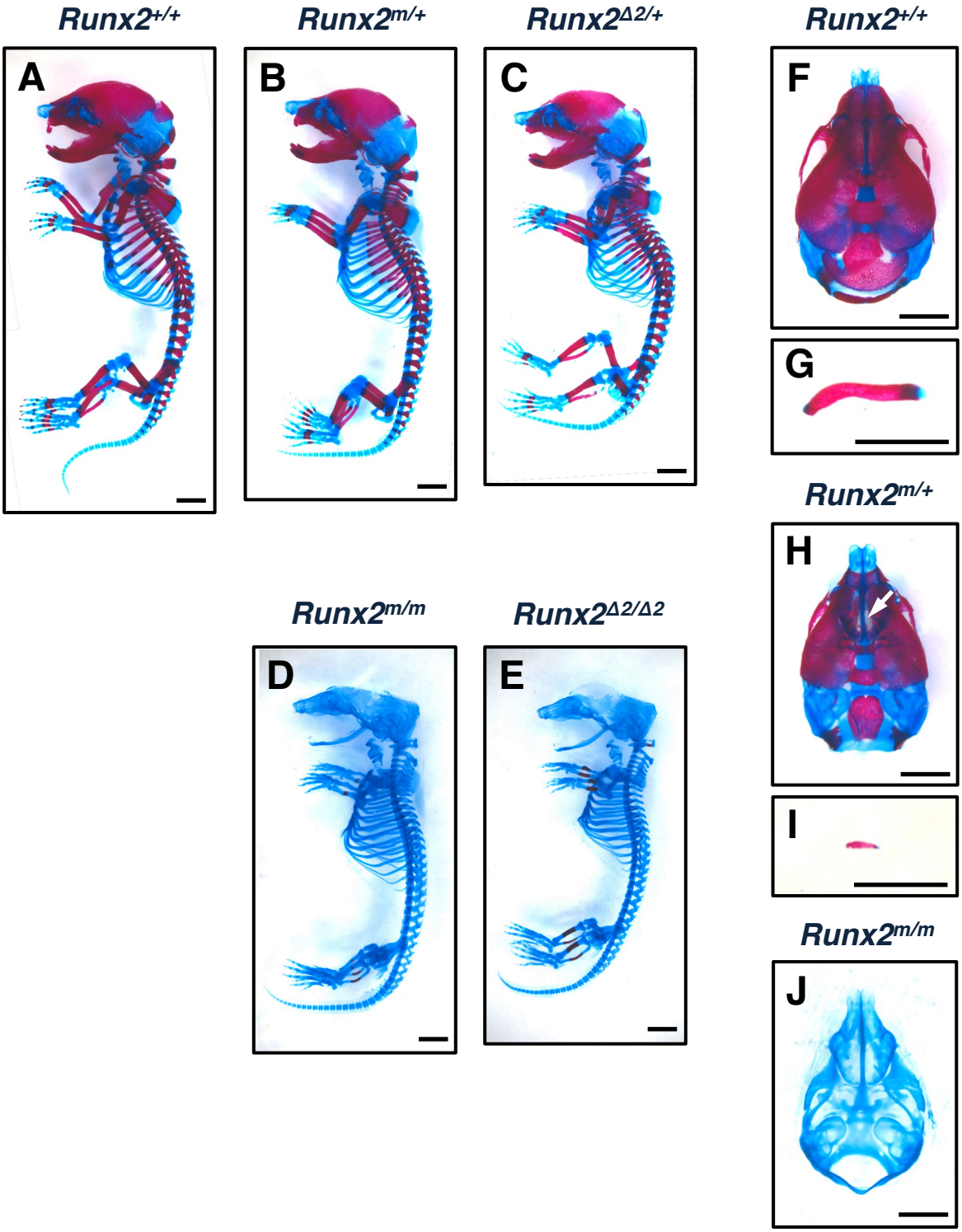
Runx2+/+
A
Runx2m/+
B
Runx2Δ2/+
C
Runx2+/+
F
G
Runx2m/+
H
I
Runx2m/m
D
Runx2Δ2/Δ2
E
Runx2m/m
J

Figure 3

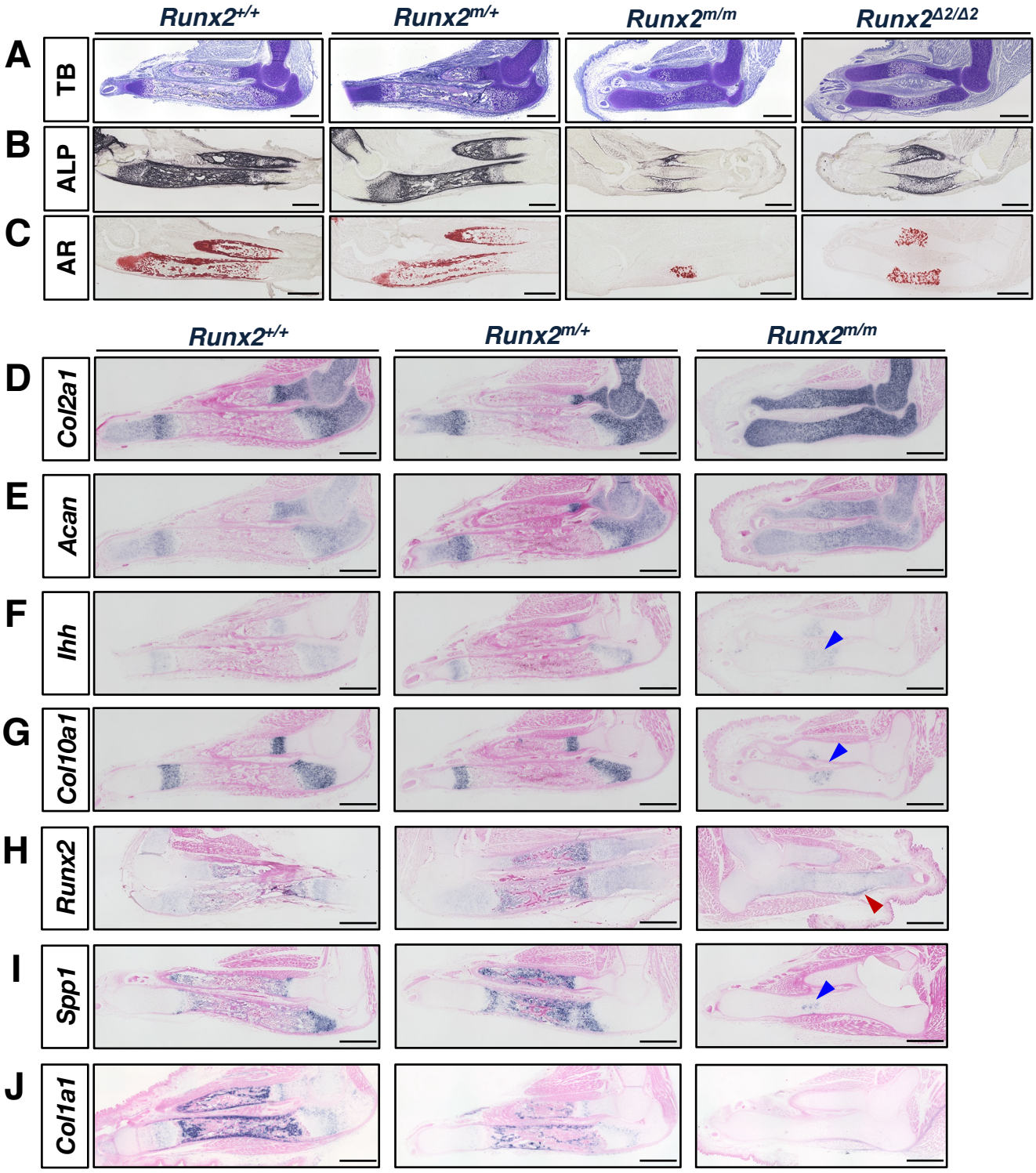
Runx2+/+
Runx2m/+
Runx2m/m
Runx2Δ2/Δ2
A
TB
B
ALP
C
AR
Runx2+/+
Runx2m/+
Runx2m/m
D
Col2a1
E
Acan
F
Ihh
G
Col10a1
H
Runx2
I
Spp1
J
Col1a1

Figure 4

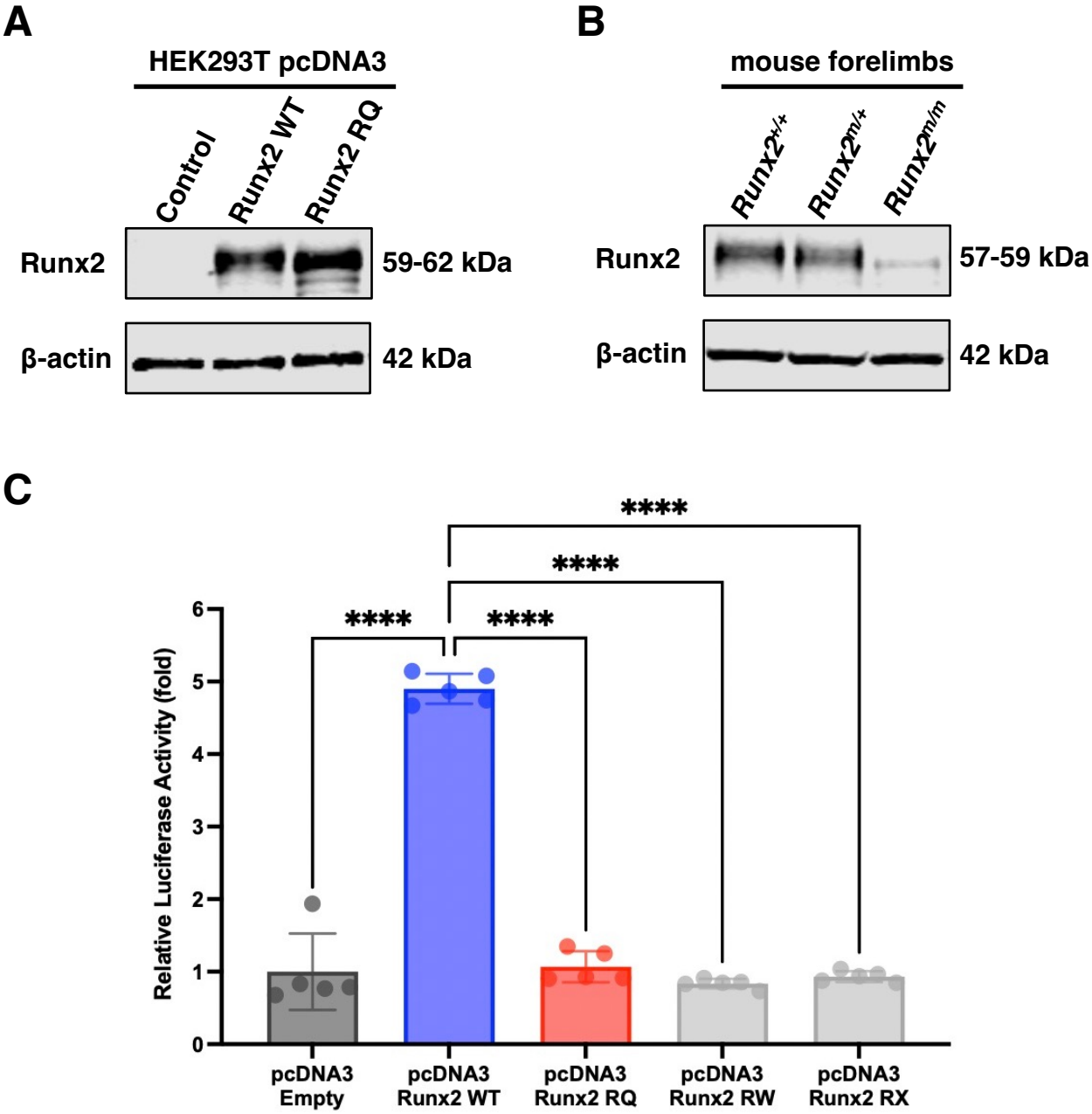
A
HEK293T pcDNA3
Control
Runx2 WT
Runx2 RQ
Runx2
59-62 kDa
β-actin
42 kDa
B
mouse forelimbs
Runx2+/+
Runx2m/+
Runx2m/m
Runx2
57-59 kDa
β-actin
42 kDa
C
****
****
****
****
Relative Luciferase Activity (fold)
0
1
2
3
4
5
6
pcDNA3 Empty
pcDNA3 Runx2 WT
pcDNA3 Runx2 RQ
pcDNA3 Runx2 RW
pcDNA3 Runx2 RX

Figure 5

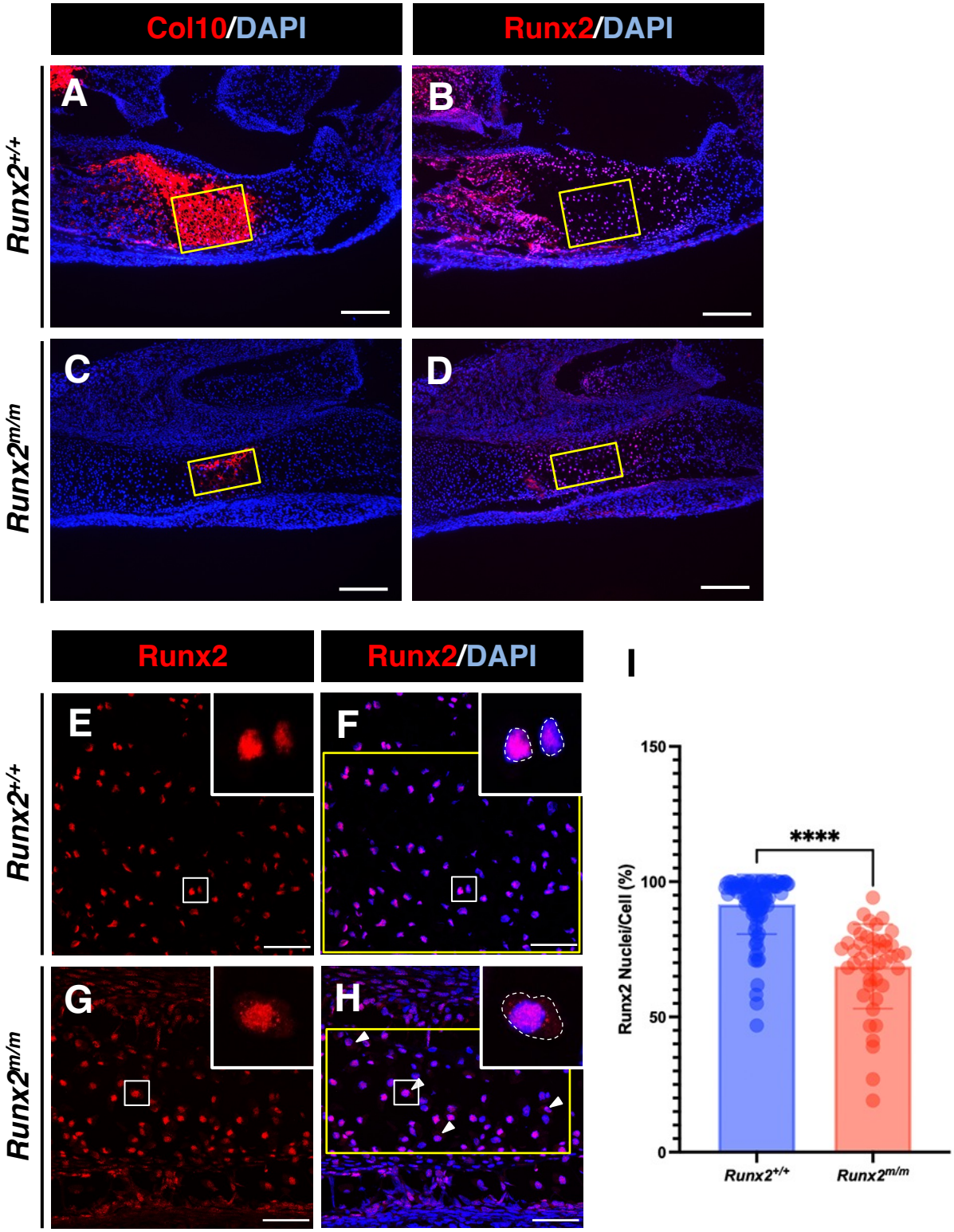
Col10/DAPI
Runx2/DAPI
A
B
C
D
Runx2+/+
Runx2m/m
Runx2
Runx2/DAPI
E
F
G
H
I
Runx2 Nuclei/Cell (%)
150
100
50
0
****
Runx2+/+
Runx2m/m

Figure 6

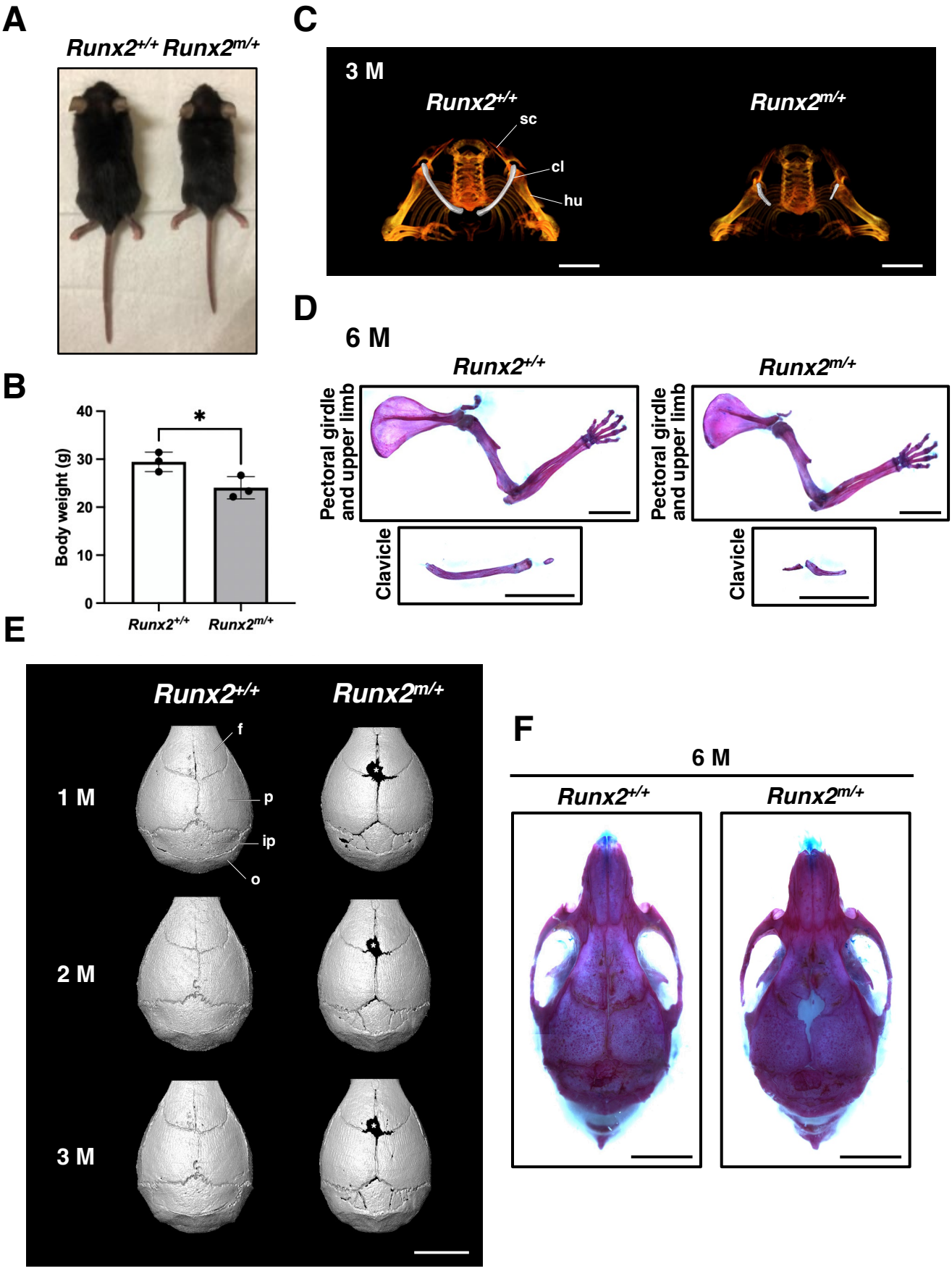
A
Runx2+/+ Runx2m/+
B
Body weight (g)
40
30
20
10
0
*
Runx2+/+
Runx2m/+
C
3 M
Runx2+/+
Runx2m/+
sc
cl
hu
D
6 M
Runx2+/+
Runx2m/+
Pectoral girdle and upper limb
Clavicle
E
Runx2+/+
Runx2m/+
1 M
2 M
3 M
f
p
ip
o
F
6 M
Runx2+/+
Runx2m/+

Figure 7

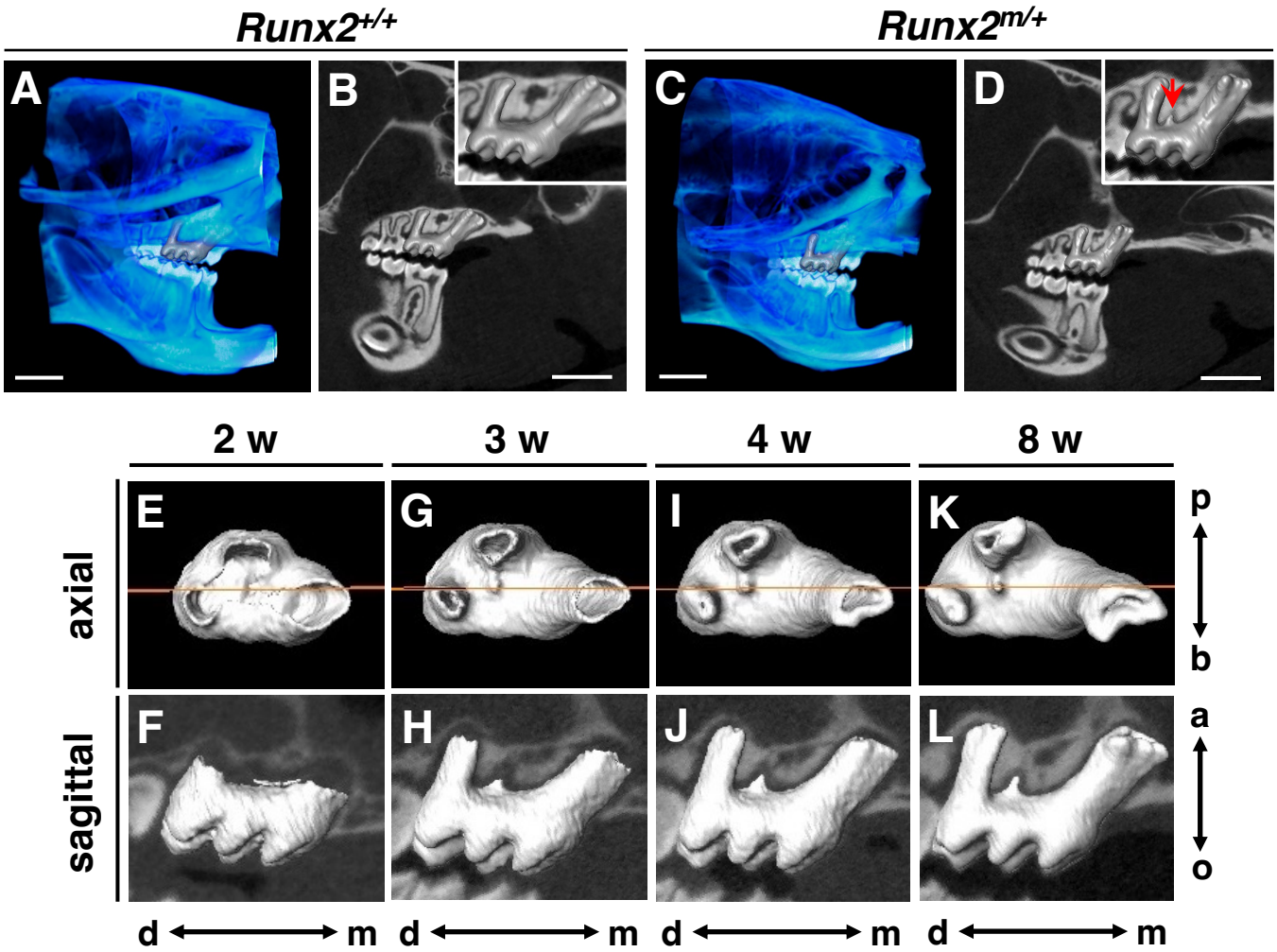
Runx2+/+
Runx2m/+
A
B
C
D
2 w
3 w
4 w
8 w
axial
sagittal
E
G
I
K
F
H
J
L
p
b
a
o
d
m

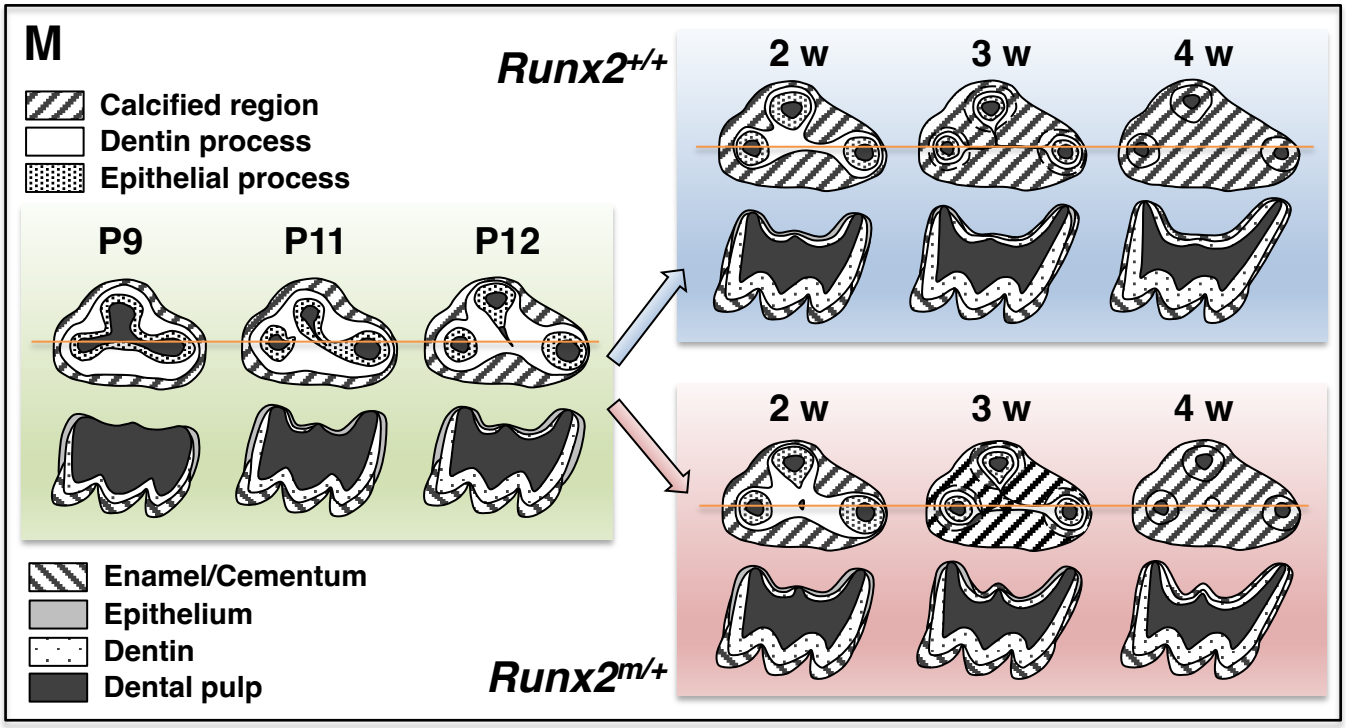
M
Calcified region
Dentin process
Epithelial process
P9
P11
P12
Enamel/Cementum
Epithelium
Dentin
Dental pulp
Runx2+/+
Runx2m/+
2 w
3 w
4 w